Inorganic Chemistry

Article

pubs.acs.org/IC

New Insights into Crystallite Size and Cell Parameters Correlation for ZnO Nanoparticles Obtained from Polyol-Mediated Synthesis

Isabelle Trenque, Stéphane Mornet, Etienne Duguet, and Manuel Gaudon*

CNRS, Université de Bordeaux, ICMCB, UPR 9048, 33600 Pessac, France

ABSTRACT: ZnO nanocrystals were prepared from polyol-mediated synthesis. Two key parameters, that is, the zinc precursor concentration and the alcohol mixture chosen as synthesis medium, were varied. The increase of the precursor concentration and the decrease of the permittivity of the alcohol mixture were shown to favor the crystallite growth, leading to crystallite sizes ranging from 5 to 35 nm. The aggregation behavior of the nanocrystal units to form or not polycrystalline spheres, depending on the van der Walls interaction density, was shown and explained. Every sample was accurately characterized by X-ray diffraction; cell parameters were extracted from full pattern matching refinements. A clear correlation between crystallite size and cell parameters, that is, an asymptotic decrease of *a* and *c* cell parameters versus the crystallite size, was established. A simple model was also successfully developed to interpret the as-established correlation.

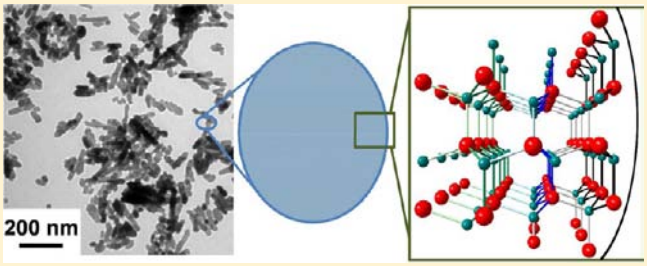

INTRODUCTION

Nanocrystals (NCs) are of growing interest in material science as well as for numerous industrial applications. A type of synthesis that turned out to be well-suited for the preparation of spherical polycrystalline particles (30−500 nm in size) made of nanosized building units (5−50 nm) is the so-called polyol route. It has been initiated by the Fievet and colleagues[1−3] in the 1990s and then largely developed by Feldmann et al.[4−8]

The polyol route was especially used for the elaboration of ZnO NCs with high purity/homogeneity and tunable particle morphology.[9] In a first step, a forced hydrolysis of zinc precursor (typically hydrated zinc acetate) is performed at temperatures of about 150−160 °C in a multivalent and high-boiling alcohol, for example, diethylene glycol (DEG, bp 246 °C). A second condensation step leads to the formation of ZnO NCs aggregated to form polycrystalline spheres. With different metallic precursors, Tseng et al. have recently obtained various shapes of the polycrystalline aggregates, for example, spheres and rods.[10] Several synthesis parameters can be varied: the composition of the polyol medium (ethylene glycol, glycerol, tetraethylene glycol), the zinc precursor source, its concentration, and its hydrolysis rate.[11−14] Most of the literature discussions dealt with the polycrystalline size, but not with the crystallite unit size. In one of our previous studies, it has been shown that polyol-mediated synthesis is also adequate to obatine A^{3+}-doped ZnO (A^{3+} = Al^{3+}, Ga^{3+}, or In^{3+}) particles for applications as TCO (transparent conductive oxides) thin films or a thermal insulation barrier.[15]

On the other hand, correlation between the crystallite size of inorganic oxides and the cell parameters, even for textbook structures, was found to be poorly reported in literature. The unit cells of most NCs are significantly different from those of the coarse-grain or single-crystal counterparts. Even if the phenomenon is well-known, it has been sparingly reported as the consequence of grain-surface relaxation (GSR effect). Stoichiometric effects related to vacancies or interstitial atoms are generally cited.[16−22] Kremenovic et al. studied nanostructured NiO/Ni composites and observed that the GSR effect connected to the displacement of atoms next to the surface of a grain from the equilibrium position is not usually considered even if this effect seems to be important.[23]

In this study, ZnO NCs were prepared from polyol-mediated synthesis using zinc acetate as precursor. The zinc precursor concentration and the composition of the DEG/hexanol mixtures were independently varied. The particle morphologies were investigated using TEM microscopy, and the crystallite size and cell parameters were extracted from X-ray diffraction analyses. Considering a GSR effect connected to the displacement of atoms next to the grain surface due to the decrease of the surface atom coordination number (bond cut), a model based on the bond valence model[24,25] was developed to explain the observed correlation between the unit cell parameters and the crystallite dimension.

EXPERIMENTAL SECTION

Suspensions of Highly Dispersed ZnO NCs. ZnO colloids were obtained through polyol-mediated precipitation, that is, forced hydrolysis at 170 °C of zinc acetate in DEG. In a typical procedure, a known amount of zinc acetate dihydrate (Sigma, ≥99%) was first dissolved in a known volume of DEG (Sigma, 99%). After heating up the solution to 160 °C for 1 h under stirring in a Pyrex round-bottom flask fitted with a reflux column, the precipitation of ZnO crystallites occurred. The solid phase was recovered by centrifugation and washed with ethanol.

The effects on the morphology of the metal cation concentration and of the chemical composition of the alcoholic medium were

Received: August 22, 2013
Published: October 25, 2013

   dx.doi.org/10.1021/ic402152f | *Inorg. Chem.* 2013, 52, 12811−12817

investigated. Thus, syntheses were performed, on one side, with various Zn^{2+} concentrations: 0.05, 0.1, 0.5, and 0.9 M in pure DEG, and, on the other side, with a fixed Zn^{2+} concentration (0.1 M) in various DEG/hexanol mixtures, with 1-hexanol (Sigma, 99%) fractions of 0, 50, 75, 90, and 100 vol %.

Characterization of the ZnO Particles/Suspensions. *Electron Microscopy.* The size and the morphology of the so-obtained particles were evaluated by scanning electron microscopy (SEM) and transmission electron microscopy (TEM). The SEM micrographs were recorded with a HITACHI 4500-I apparatus fit out with a field emission gun (SEM-FEG) working at 3.0 kV. Such equipment allows a high spatial resolution (roughly equal to 5 nm) while operating at such low accelerating voltages. TEM experiments were performed on a HITACHI H7650 equipment with a field emissive gun operating at 80 kV and a point resolution of 1 nm.

X-ray Diffraction. X-ray diffraction patterns were collected using a PANalytical X'Pert MPD PW 3040 with Cu $K\alpha_1$ radiation (λ = 1.540562 Å), and the measurements were performed in continuous scan mode with a scan step of 0.028 in the 2θ range from 20 to 80° (overnight measurements). The setup of the instrument is of Bragg–Bentano geometry with a primary monochromator Ge(111) equipped with fixed divergence and antiscattering slits. The Fullprof program was used for both full pattern matching and structural refinements by the Rietveld method.[26,27] Nevertheless, the atomic position refinements bringing no supplementary information, only the results and the conventional reliability factors (cR_p and cR_{wp}) corresponding to the full profile matching mode are herein reported. X-ray diffraction refinements using the peak profile Fullprof function n°7 (Thomson, Cox, and Hastings peak profile function) were also used to evaluate the size of the crystallites. IRF (instrumental resolution function) was defined using very similar collecting parameters than for the samples on the LaB_6 "SRM660a" standard material. The shape of the crystallites deduced the application of an anisotropic size-strain model (platelet-type: −1 or needle-type: +1 model), which was performed empirically, that is, testing one by one different anisotropic axes, and finally selecting the shape-type and the deformation axis, which lead to the smallest reliability factors (the best fit). With Fullprof software, the parameter relative to the anisotropy intensity is the "LorSiz". Size-Model (*xxx*) ± 1 means: the deformation axis is the (*xxx*) axis (a "flattening" axis for platelet-type model: +1 or an elongation axis for needle-type shape: −1.)

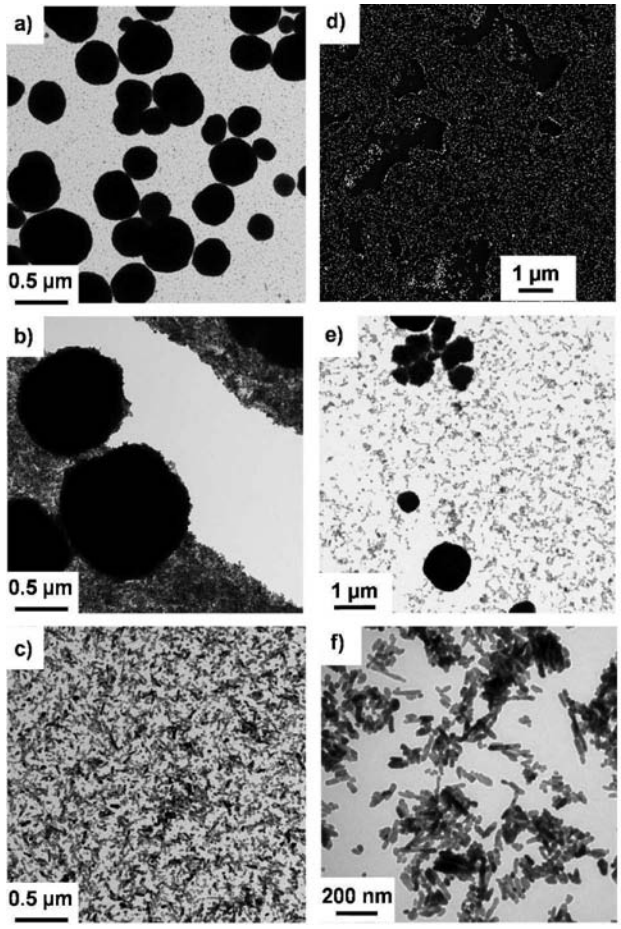

Figure 1. Typical SEM and TEM micrographs of ZnO particles showing the spherical aggregates and dispersed nanocrystallites, as a function of the zinc precursor concentration used in the polyol-mediated synthesis in pure DEG: 0.1 M (a, d), 0.5 M (b, e), and 0.9 M (c, f).

RESULTS AND DISCUSSION

Effect of the Zinc Cation Concentration. TEM and SEM images on the primary particles obtained using different Zn^{2+} concentrations in DEG show a drastic evolution of morphology (Figure 1). Spherical polycrystalline aggregates were obtained in the ethanol suspensions for low Zn^{2+} concentrations, for example, 0.05 and 0.1 M (Figure 1a,d). Statistical analyses performed on SEM images showed an average diameter of about 310 nm with a quite narrow size distribution (the particles ranging between 150 nm for the 10% smallest ones and 480 nm for the 10% biggest ones). Increasing the ZnO precursor concentration up to 0.5 M induced two important changes: (i) the average diameter of the spherical aggregates increased up to 800 nm, and (ii) "softly agglomerated" crystallites appeared besides the aggregates (Figure 1b,e). The latter phenomenon was drastically enhanced when increasing once again the precursor concentration up to 0.9 M, giving agglomerate-free dispersions (Figure 1c,f). The increase of the precursor concentration induced a significant decrease of the spherical agglomerates' cohesion strength until the complete "dispersion" of the constituting crystallites in the ethanol suspensions. The obtaining of less coherent agglomerates with the metal cation concentration increase was actually due to an increase of the constituting crystallite size (Table 1). First, it has to be noted that the crystallites can exhibit anisotropic shapes in resonance with the würtzite structure, needing hence to make pattern refinements with anisotropic peak profile function. As illustration, the pattern refinement of the 0.1 M sample using an isotropic or anisotropic model along the (110) axis is reported in Figure 2 (experimental, calculated and differential spectra are both represented). The zoom-in on some characteristic 2θ angle range of the differential spectra illustrates the importance of getting correct refinement quality and low reliability factors to perform the refinements with an anisotropic peak profile model. The crystallite sizes as well as the crystalline anisotropy are both deeply impacted by the precursor concentration. As shown in Table 1, the anisotropic shape of the crystallite changed dramatically from (110) needle to (110) platelet; that is, the crystallite exhibited an opposite morphology, when the precursor concentration varied from 0.1 to 0.5 M. Additionally, the crystallite size increased from 7 to 21 nm along the (110) axis and continued to expand while a higher concentration (0.9 M) was used. The progressive increase of the crystallite size with the precursor concentration was also evidenced from the progressive reduction of the peak width (Figure 3).

The concentration of metal cation during the precipitation controls the thermodynamic balance between the nucleation of the crystallites, the growth of the pre-existing crystallites, and the aggregation of the crystallites. Here, the precipitation

dx.doi.org/10.1021/ic402152f | Inorg. Chem. 2013, 52, 12811–12817

Table 1. Cell Parameters and Grain Sizes in the (100) and (002) Directions of the ZnO Nanoparticles Obtained from Various Initial Zn^{2+} Concentrations in DEG

concentration in cation (M)	grain size (100) (nm)	grain size (002) (nm)	*a* (A)	*c* (A)	size-model (110)	LorSiz	cR_p (%)	cR_{wp} (%)
0.05	8.2	6.7	3.2513(6)	5.2146(9)	−1	5.95	4.58	5.62
0.1	7.9	6.8	3.2515(3)	5.2121(5)	−1	5.06	3.99	4.97
0.5	15.3	20.6	3.25067(6)	5.2075(1)	1	2.39	6.08	7.18
0.9	23.3	33.4	3.25027(6)	5.2070(1)	1	1.84	9.63	11.2

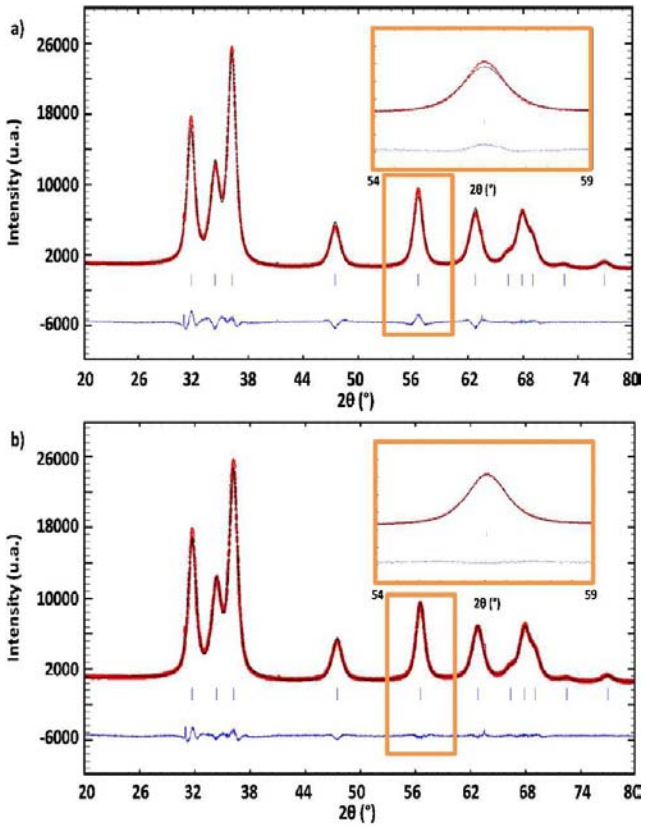

Figure 2. Experimental, calculated and differential XRD patterns illustrating the pattern matching quality for ZnO compounds obtained using a Zn precursor concentration in DEG equal to 0.1 M: isotropic peak profile model (a) and anisotropic (110 vector) peak profile model (b).

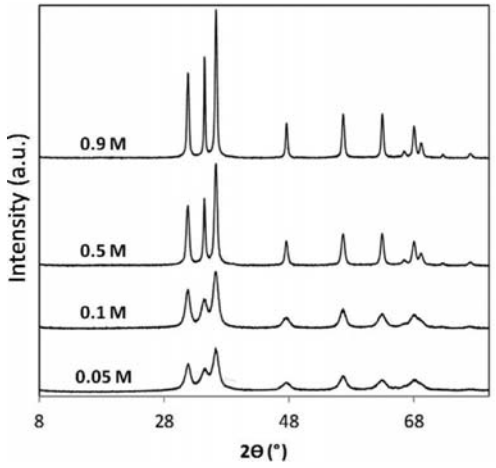

Figure 3. XRD patterns of ZnO particles as a function of Zn precursor concentration in pure DEG.

performed in concentrated medium favored the crystallite growth. It can be supposed that, even if the increase of the concentration, and so the supersaturation reached before the germination step, tends to increase the nucleation velocity (La Mer model[28,29]), the ratio between the number of nuclei and the available Zn^{2+} cations in solution decreases with increasing Zn^{2+} precursor concentration, leading thus to larger crystallites at the end of the nucleation−growth process. The increase of the crystallite size induces a collapse of the van der Walls interactions between crystallites responsible of the overall cohesion of the agglomerates, the interface (contact) area (between two crystallites in the spherical aggregates) per volume unit becoming smaller and smaller. Thus, suspensions of highly dispersed NCs can be readily prepared from a high Zn^{2+} concentration in DEG.

Effect of the Alcohol Nature. This study was conducted in a symmetric way to that related to the influence of the precursor concentration. TEM-extracted morphologies obtained for various hexanol concentrations in DEG are shown in Figure 4. In parallel, the crystallite size was calculated from X-ray pattern refinements; diffractograms were superimposed (Figure 5). The refinement results are reported in Table 2. Briefly, the replacement of DEG by hexanol had the same effect as the increase of the precursor concentration in DEG, that is, an increase of the crystallite sizes leading to spherical aggregates less and less cohesive until the achievement of dispersion at the

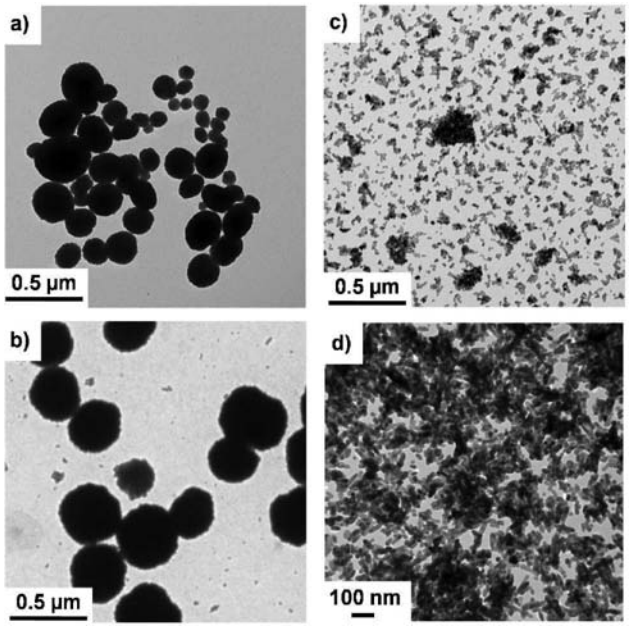

Figure 4. Typical TEM micrographs of ZnO particles showing the spherical aggregates and dispersed nanocrystallites, as a function of the fraction of hexanol in the DEG/hexanol mixture used as synthesis medium for a Zn precursor concentration of 0.1 M: 0 (a), 50 (b), 75 (c), and 90 vol % (d).

dx.doi.org/10.1021/ic402152f | *Inorg. Chem.* 2013, 52, 12811−12817

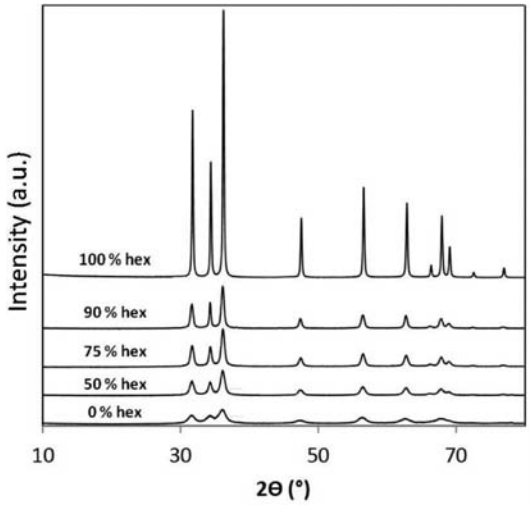

Figure 5. XRD patterns of the ZnO particles as a function of the fraction of hexanol in the DEG/hexanol mixture used as synthesis medium for a Zn precursor concentration of 0.1 M.

NCs level. Up to a hexanol concentration equal to 50 vol %, the net increase of the crystallite size remained low: from about 7 nm for the synthesis performed in pure DEG to 11 nm for the 50−50 vol % DEG−hexanol medium. The spherical aggregates' morphology was also weakly impacted; a slight growth of the aggregates, positively correlated to the constituting crystallite size, can be nevertheless evidenced between panels (a) and (b) in Figure 4. The X-ray diffraction refinements showed that, with 75 or 90 vol % of hexanol, the crystallite size increased to about 15 nm or about 25 nm, respectively. The agglomerates had disappeared to give way to crystallites that were found isolated or grouped to form small agglomerates of few tenths of a nanometer (Figure 4c). It can be noted that the crystallite shape tended to be changed as a function of the polyol medium used, as it was previously shown as a function of the metal precursor concentration.

Here, it is obvious that the parameter directly governing the nucleation−growth thermodynamics is the medium permittivity (ε_r): 31.7 and 13.3 for DEG and hexanol, respectively. Whatever, the obtaining of less cohesive agglomerates with the higher hexanol concentrations is due, like in the previous experiments, to a decrease of the van der Walls interactions related to an increase of the average crystallite size.

Correlation between Crystallite Size and Cell Parameter. By varying the key parameters, that is, the composition of the alcohol medium or concentration of the metal precursor, the polyol-mediated syntheses allowed controlling the crystallite size and shape in the nanometer range. The pattern matching of the X-ray diffraction spectra using the (110) anisotropic shape allowed independently and accurately the characterization of both *a* and *c* cell parameters. Bringing together the results obtained in the two previous studies, the evolution of the *c* and *a* cell parameters versus the crystallite size along (002) and (100) axes are plotted in Figure 6a,b,

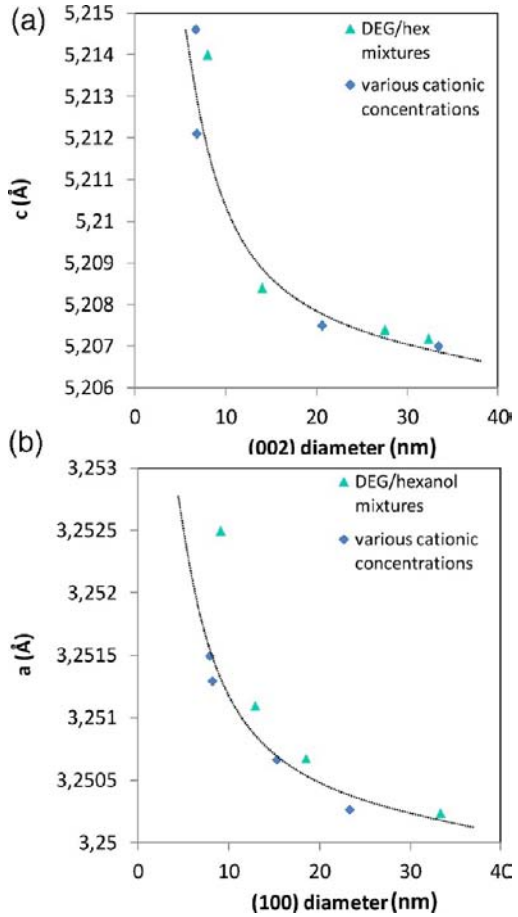

Figure 6. Cell parameters extracted from XRD pattern refinements for different ZnO compounds versus their grain diameter.

respectively. Both *a* and *c* cell parameters decreased versus the crystallite size with an evolution that can be described as a clear and monotonic asymptotic curve. A model from solid-state chemistry as the bond-valence model of Brown et al.[24,25] can help to interpret this behavior. It can be noted that, from our knowledge, such a clear observation was never reported. The modification of the ZnO average cell parameters depending on the crystallite size obviously comes from drastic modifications of the interatomic distances between the planes near the crystallite surface. One surface can be described as an area of missing bonds (with the subsequent excess of energy), and intuitively, the missing bonds around the surface atoms should cause a shortening of the bonds between these surface atoms and the atoms of the first underlayment. Indeed, the bond valence law expresses that the distance and the coordination number of an ion are linked by the equation

Table 2. Cell Parameters and Grain Sizes in the (110) and (002) Directions of the ZnO Nanoparticles Obtained from Various Initial Zn^{2+} Concentrations in DEG

% vol hexanol	grain size (100) (nm)	grain size (002) (nm)	*a* (A)	*c* (A)	size-model (110)	LorSiz	cR_p (%)	cR_{wp} (%)
0	9.1	8.0	3.2525(7)	5.214(1)	−1	3.97	4.37	6.39
50	12.9	14.0	3.2511(1)	5.2084(2)	1	0.93	7.31	9.18
90	18.5	27.5	3.25068(7)	5.2074(2)	1	2.55	7.03	8.21
100	33.3	32.3	3.25024(2)	5.20718(4)	−1	0.22	3.75	5.30

dx.doi.org/10.1021/ic402152f | *Inorg. Chem.* 2013, 52, 12811−12817

$$V = \sum_{i=1}^{n} bv_i = \sum_{i=1}^{n} \exp((r_0 - L_i)/0.37) \quad (1)$$

where V is the valence of the ion (equal to the oxidation degree modulus: here, $V = 2$ for Zn^{2+} and O^{2-}), bv_i is the bond valence of each bond implying the central ion, r_0 is an empirically determined parameter characteristic of the A–X bond (r_0 is tabulated equal to 1.704 Å for Zn^{2+}–O^{2-} bond), and L_i is the length of each i bond of the first coordination sphere. The valence is then a function of the number of bond lengths; when the coordination number i decreases, each bond length should also decrease to maintain the V value to 2 for each ion of the ZnO würtzite structure.

A Pauling–Brown bond relaxation approach was attempted to try to explain the variation of the cell parameters versus the crystallite size. In this approach, in a first step, we tried to identify "natural" surface planes considering that the most easy and only acceptable way (on a thermodynamic point of view) to cut the tetrahedral sites is to cut only one bond on its four ones, that is, to keep three neighbors for the O^{2-} or Zn^{2+} surface cations. From this hypothesis, it is easy to identify the (010) or (100) planes, as represented in Figure 7, as natural

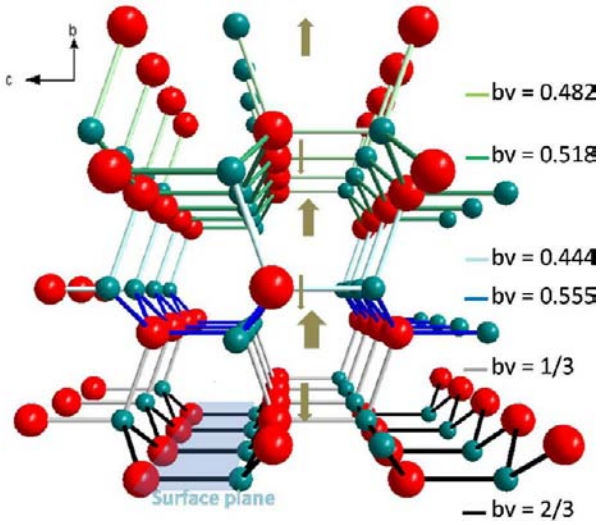

Figure 7. Calculation of the bond valences (bv) for bonds of successive layers from the surface to the bulk considering, as an illustration, the section plane perpendicular to the b axis.

cutting planes. A second step is to attribute the bond valence of the successive bond layers from the surface to the bulk, layer by layer, in order to respect the ions' V valence value ($V = 2$). Hence, with the cutting plane considered, for the "surface" bonds represented in bold black in Figure 7, due to the missing of one Zn^{2+} for each surface O^{2-}, and one O^{2-} for each surface Zn^{2+}, all bond valences (bv_i) have to equal 2/3. The second half-layer of ions gets four neighbors: two of them are surface ions, that is, exchanging with the considered ion a flux of an electronic charge of 2/3; then the two other bonds have to get a valence of 1/3. This second sublayer of bonds with $bv = 1/3$ is represented in light gray. The reasoning was extended to the successive sublayers from the surface to the core of the particles and led to the bond valence values reported in Figure 7. For example, for the second layer with bonds in blue, the first half-layer (bonds in deep blue) gets a bond with $bv = 0.555$ and the second half-layer (bonds in light blue) gets a bond with $bv = 0.444$. Very quickly, the calculated bv values are converging at the bulk bv value of 2, demonstrating the validity of the applied model.

From eq 1, the bv_i values are inversely proportional to the bond length. This equation was used to calculate the bond length of the successive half-layers from the surface (Figure 8a). In accordance with the calculated bond lengths, some shortenings or some increase of the interlayer distances have to occur; the relaxation displacement of each layer is represented by arrows in Figure 7. Actually, the half-layers are alternatively thicker or thinner. In a next step, it is possible to calculate each layer thickness, from the sum of the two corresponding half-layers, adding up the projection along the axis perpendicular to the surface plane (Figure 8b,c). With the consideration of an almost regular tetrahedral shape for each site (with bond angles of 109°), that is, not taking into account the relaxation atomic displacements, the layer thickness, for each layer, can be derived from eq 2

$$\text{Layer Thickness} = \left(\frac{1}{2} \times \cos(19°) * bl_1 + \cos(19°)\right) * bl_2 \quad (2)$$

where bl_1 and bl_2 are the bond length of the first half-layer (bonds represented in Figure 7 in deep colors) and the bond length of the second half-layer (in light colors), respectively.

From this mathematical treatment, the layer thickness versus their number is represented in Figure 8b, showing the sum for each layer thickness of both half-layer components. A zoom-in on the top of the histogram curve clearly shows the asymptotic decrease of the layer thickness from the surface to the core of the crystallites (Figure 8c).

Considering that the cutting plane perpendicular to each cell axis can be modeled like the cutting plane represented in Figure 7, a last mathematical treatment allowed calculating the c or a average parameters versus the crystallite size from the thickness of the layers depending on their position from the surface. The evolution of the elongation factor described as c_{exp}/c_{bulk} versus the crystallite size brought to the fore a similar evolution: an asymptotic decrease extended on the same crystallite size range as the one extracted experimentally from the X-ray pattern refinements (Figure 9). It seems that the "Pauling–Brown" approach used to simulate the atomic displacements issued from the bond missing on the crystallite surface is appropriate enough to predict the dependence of cell parameters versus crystallite size in the würtzite structure. Actually, the curve shape is perfectly predicted as shown in the Figure 9 curve; nevertheless, the a and c numerical values are slightly overestimated by our model. An explanation could be that no pending bonds are taken into account in our model, whereas the zinc oxide can interact with the gaseous atmosphere, forming pending bonds (with hydroxyl or carbonyl groups). Consequently, a decrease of some surface bond valences in comparison with our model can occur due to the zinc oxide and atmosphere interaction.

CONCLUSIONS

We reported on a simple and cheap method for the elaboration of ZnO NCs with crystallite size as well as the aggregation behavior that can be controlled. The method already known as polyol-mediated synthesis was here optimized by the systematic study of the zinc precursor concentration and the composition of the DEG/hexanol mixture chosen for the forced hydro-condensation step. The lattice parameter values showed a

dx.doi.org/10.1021/ic402152f | Inorg. Chem. 2013, 52, 12811–12817

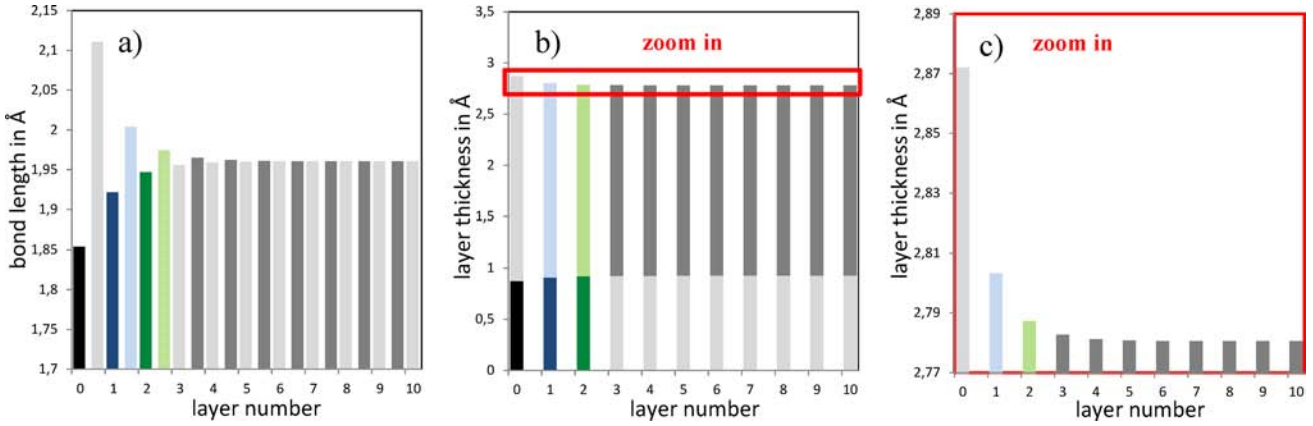

Figure 8. Calculation of the bond length and layer thickness (from bond projection on the vertical axis to the surface plane) for successive layers: the layers are numbered in growing order (from 0 to *n*) from the surface layer to the bulk. In (a) can be distinguished the variation of each half-layer, whereas, in (b) and (c), the half-layers are cumulated in order to draw the evolution of the successive layers.

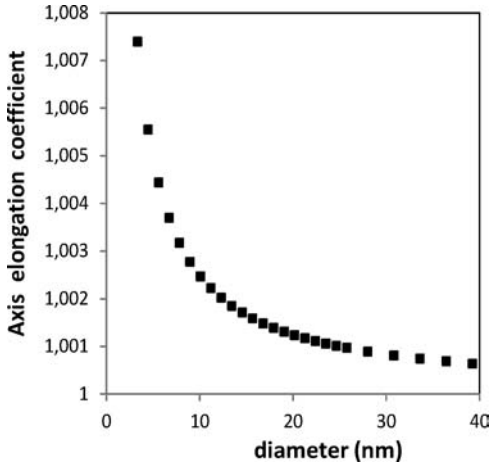

Figure 9. Expansion coefficient of the cell parameter perpendicular to the section plane calculated considering the bond valences for successive planes from the surface to the bulk versus grain diameter.

significant size effect: an exponential increase of both *a* and *c* cell parameters while the crystallite size decreases was observed. This was interpreted as a grain-surface relaxation effect in nanocrystals. On the basis of the bond valence law, a simple model was successfully proposed, leading to a satisfying fit of the experimental cell parameters curve versus crystallite size. It was shown that, even if the evolution of cell parameters evidenced in this paper is obviously not universal and depended on the nature of the surface plane, the compound crystallographic structure, the occurrence or not of hydrated water or hydroxyl group on the surface, etc., the Pauling–Brown approach developed here can be applied in a universal way to predict the evolution of cell parameters versus crystallite size.

AUTHOR INFORMATION

Corresponding Author

*E-mail: gaudon@icmcb-bordeaux.cnrs.fr.

Notes

The authors declare no competing financial interest.

ACKNOWLEDGMENTS

The Conseil Régional d'Aquitaine and the Agence Nationale pour la Recherche (project ANR-A2010 JCJC 0805 01) are gratefully acknowledged.

REFERENCES

(1) Jezequel, D.; Guenot, J.; Jouini, N.; Fievet, F. *J. Mater. Res.* **1994**, *10*, 77.
(2) Toneguzzo, P.; Viau, G.; Acher, O.; Guillet, F.; Fievet-Vincent, F.; Fievet, F. *J. Mater. Sci.* **2000**, *35*, 3767.
(3) Toneguzzo, P.; Viau, G.; Acher, O.; Guillet, F.; Fievet-Vincent, F.; Fievet, F. *Adv. Mater.* **1998**, *10*, 1032.
(4) Feldmann, C. *Scr. Mater.* **2001**, *44*, 2193.
(5) Feldmann, C.; Jungk, H. O. *Angew. Chem., Int. Ed.* **2001**, *40*, 359.
(6) Feldmann, C. *Adv. Funct. Mater.* **2003**, *13*, 101.
(7) Schmitt, P.; Brem, N.; Schunk, S.; Feldmann, C. *Adv. Funct. Mater.* **2011**, *21*, 3037.
(8) Jungk, H. O.; Feldmann, C. *J. Mater. Res.* **2000**, *15*, 2244.
(9) Hu, X.; Gong, J.; Zhang, L.; Yu, J. C. *Adv. Mater.* **2008**, *20*, 4845.
(10) Tseng, Y.-K.; Chuang, M.-H.; Chen, Y.-C.; Wu, C.-H. *J. Nanotechnol.* **2012**, Article ID 712850.
(11) Poul, L.; Ammar, S.; Jouini, N.; Fievet, F.; Villain, F. *J. Sol-Gel Sci. Technol.* **2003**, *26*, 261.
(12) Dakhlaoui, A.; Jendoubi, M.; Smiri, L.; Kanaev, A.; Jouini, N. *J. Cryst. Growth* **2009**, *311*, 3989.
(13) Chieng, B.; Loo, Y. *Mater. Lett.* **2012**, *73*, 78.
(14) Zhang, Q.; Chou, T.; Russo, B.; Jenekhe, S.; Cao, G. *Adv. Funct. Mater.* **2008**, *18*, 1654.
(15) Trenque, I.; Mornet, S.; Duguet, E.; Gaudon, M. *Mater. Res. Bull.* **2013**, *48*, 1155.
(16) Edelstein, A. S.; Murday, J. S.; Rath, B. B. *Prog. Mater. Sci.* **1997**, *42*, 5.
(17) Valiev, R. Z.; Islamgaliev, R. K.; Alexandrov, J. V. *Prog. Mater. Sci.* **2000**, *45*, 103.
(18) Gleiter, H. *Acta Mater.* **2000**, *48*, 1.
(19) Lu, K.; Zhao, Y. H. *Nanostruct. Mater.* **1999**, *12*, 559.
(20) Liu, X. D.; Zhang, H. Y.; Lu, K.; Hu, Z. Q. *J. Phys.: Condens. Matter* **1994**, *6*, 497.
(21) Eastman, J. A.; Fritzsimmons, M. R.; Thompson, L. J. *Philos. Mag. B* **1992**, *66*, 667.
(22) Bakker, H.; Zhou, G. F.; Yang, H. *Prog. Mater. Sci.* **1995**, *39*, 159.
(23) Kremenovic, A.; Janca, B.; Ristic, M.; Vucinic-Vasic, M.; Rogan, J.; Pacevski, A.; Antic, B. *J. Phys. Chem. C* **2012**, *116*, 4356.
(24) Brown, I. D. *The Chemical Bond in Inorganic Chemistry: The Bond Valence Model*; Oxford University Press: Oxford, U.K., 2002.
(25) Brown, I. D.; Altermatt, D. *Acta Crystallogr.* **1985**, *41*, 244.
(26) Rietveld, H. M. *Acta Crystallogr.* **1967**, *22*, 151.

(27) Rietveld, H. M. *J. Appl. Crystallogr.* **1969**, *2*, 65.
(28) La Mer, V. K.; Dinegar, R. H. *J. Am. Chem. Soc.* **1950**, *72*, 4847−4854.
(29) Tao, A. R.; Sinsermsuksakul, P.; Yang, P. *Angew. Chem.* **2006**, *118*, 4713.